



CLIC – Note – 942

DESIGN AND SYSTEM INTEGRATION OF THE SUPERCONDUCTING WIGGLER MAGNETS FOR THE CLIC DAMPING RINGS

Daniel Schoerling ^{1,2}, Fanouria Antoniou ², Axel Bernhard ³, Alexey Bragin ⁴,
Mikko Karppinen ², Remo Maccaferri ², Nikolay Mezentsev ⁴, Yannis Papaphilippou ²,
Peter Peiffer ³, Robert Rossmann ³, Giovanni Rumolo ², Stephan Russenschuck ²,
Pavel Vobly ⁴ and Konstantin Zolotarev ⁴

¹Technische Universität Bergakademie Freiberg, Germany

²CERN, Switzerland

³KIT, Karlsruhe Institute of Technology, Karlsruhe, Germany

⁴Budker Institute of Nuclear Physics SB RAS, Novosibirsk, Russia

Abstract

To achieve high luminosity at the collision point of the Compact Linear Collider (CLIC) the normalized horizontal and vertical emittances of the electron and positron beams must be reduced to 500 nm and 4 nm before the beams enter the 1.5 TeV linear accelerators. An effective way to accomplish ultra-low emittances with only small effects on the electron polarization is using damping rings operating at 2.86 GeV equipped with superconducting wiggler magnets. This paper describes a technical design concept for the CLIC damping wigglers.

Geneva, Switzerland
May 2012



Design and System Integration of the Superconducting Wiggler Magnets for the CLIC Damping Rings

Daniel Schoerling,^{1,2} Fanouria Antoniou,² Axel Bernhard,³ Alexey Bragin,⁴ Mikko Karppinen,² Remo Maccaferri,² Nikolay Mezentsev,⁴ Yannis Papaphilippou,² Peter Peiffer,³ Robert Rossmannith,³ Giovanni Rumolo,² Stephan Russenschuck,² Pavel Vobly,⁴ and Konstantin Zolotarev⁴

¹*Technische Universität Bergakademie Freiberg, Germany*

²*CERN, Switzerland*

³*KIT, Karlsruhe Institute of Technology, Karlsruhe, Germany*

⁴*Budker Institute of Nuclear Physics SB RAS, Novosibirsk, Russia*

To achieve high luminosity at the collision point of the Compact Linear Collider (CLIC) the normalized horizontal and vertical emittances of the electron and positron beams must be reduced to 500 nm and 4 nm before the beams enter the 1.5 TeV linear accelerators. An effective way to accomplish ultra-low emittances with only small effects on the electron polarization is using damping rings operating at 2.86 GeV equipped with superconducting wiggler magnets. This paper describes a technical design concept for the CLIC damping wigglers.

PACS numbers: 84.71.Ba, 41.20.Gz, 41.75.Ht, 29.20.Dk, 29.20.Ej

I. INTRODUCTION

CLIC (Compact Linear Collider) is a study for an electron-positron collider in the TeV range. Fundamental physics data complementary to the Large Hadron Collider (LHC) and lower-energy linear electron-positron colliders may be obtained with measurements at the collision point of CLIC. Detailed information on the CLIC design study can be found in [1].

To achieve the required luminosity at the collision point of CLIC, the normalized horizontal emittance including the effect of intrabeam scattering has to be less than 500 nm rad before entering the linear collider. Intrabeam scattering is a small angle multiple Coulomb scattering effect [3], which causes a beam emittance growth. Moreover, the normalized vertical zero-current emittance has to be 4 nm rad and the normalized longitudinal zero-current emittance has to be 6000 eVm. For the reduction of the emittance, damping rings are foreseen. Both the electron and the positron beams enter first the pre-damping rings and afterwards the main damping rings. The damping rings will be racetrack shaped rings with 26 wigglers placed in each straight section. The horizontal equilibrium emittance is designed to be around one order of magnitude smaller than in other planned or built rings (Fig. 1), which can be only achieved with superconducting damping wiggler magnets.

The baseline design foresees Nb-Ti superconducting wigglers. But by using the more challenging Nb₃Sn technology the magnetic flux density amplitude B_w can be increased (see Fig. 2 for the parameters of the wiggler magnets), which may open the possibility to shorten the damping rings. Moreover, the enthalpy margin for Nb₃Sn wiggler magnets with the same loadline margin as Nb-Ti wiggler magnets is larger, which will result in more stable operation. First promising tests show that Nb₃Sn wiggler magnets can reach the high magnetic flux density, but more detailed studies are required before a final

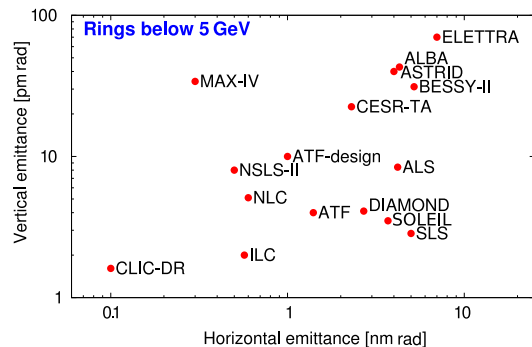


FIG. 1. Comparison of vertical versus horizontal emittances of different storage rings below 5 GeV with the CLIC damping rings [2].

decision can be taken.

To test the wiggler system with beam, two prototypes of two different concepts of superconducting wigglers are foreseen to be installed in the ANKA storage ring [4]. The operational parameters for Nb-Ti are: $B_w = 3.0$ T, 35 periods, 56 mm period length, a beam stay clear of 13 mm and a magnetic gap g of 18 mm. The design values for a Nb₃Sn wiggler magnet are (except for the magnetic flux density which is $B_w = 4.0$ T) identical. The test of the Nb₃Sn damping wiggler can be performed in the same cryostat.

The schematic layout of the cryostat is shown in Fig. 3. The essential of the design is that the vacuum chamber and superconducting coils have minimum thermal contact and that they are cooled by using separate cooling circuits. In between the vacuum chamber and the coils is a small vacuum (10^{-4} Pa) gap. The vacuum chamber is spaced to the coils by using small spacers with a low thermal conductivity. So, if the vacuum chamber receives heat load from the beam the coils are only slightly affected. The vacuum chamber with a vacuum

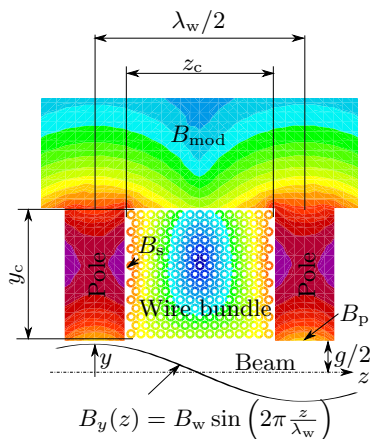


FIG. 2. Parameters of the wiggler magnets.

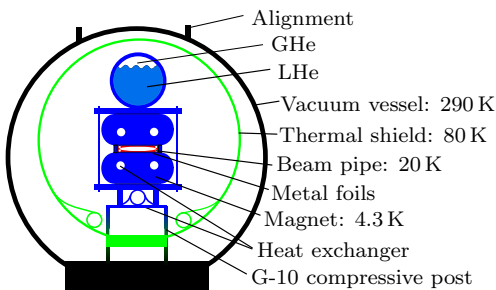


FIG. 3. Conceptual design of cryostat.

level smaller than 10^{-7} Pa [5] is cooled by gaseous helium and can be operated at temperature levels between 20 K and 80 K, cooling at 80 K would reduce the power consumption by about a factor of 5 compared to cooling at 20 K. For the positron damping ring it might be additionally necessary to coat the vacuum chambers with specialized coatings to reduce electron cloud effects (see section IV B 2). The coils are cooled by a flow of liquid helium at atmospheric pressure flowing through heat exchangers. This cooling technique reduces significantly the amount of stored helium. Since the liquid helium flows through the center of the coils the existing coils act as a rigid mechanical barrier between the vacuum and the liquid helium. Therefore, no additional pressure barrier between coils and beam vacuum as in standard wiggler magnets with bath cooling (summarized in [6]) is needed to ensure that the beam pipe is not plastically deformed in case of quench due to the mechanical load of the pressure increase caused by the vaporizing helium (usually up to 10^6 Pa). Therefore, the wiggler magnet with the proposed cooling system can be operated with the same beam stay clear but at a smaller pole distance resulting in a considerably larger magnetic field compared to bath cooled magnets because of the nonlinear magnetic flux density to gap relation given in Equation (3).

In this paper, a conceptual design for superconducting vertical and horizontal racetrack damping wiggler magnets (see Fig. 4) is presented, which allows to derive very

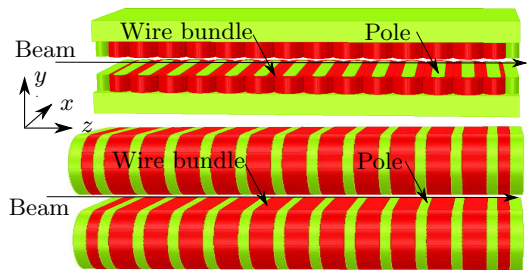


FIG. 4. Horizontal (top) and vertical (bottom) racetrack wiggler magnets.

quickly an optimized wiggler magnet design for damping rings. Moreover, a full analysis of the heat load in racetrack damping rings equipped with superconducting damping wiggler magnets in series in a racetrack damping ring is derived. The heat load analysis shows that conduction cooling has to be applied to superconducting wiggler magnets. So far, to the knowledge of the authors, all existing superconducting damping wiggler magnets are cooled by using bath cooling. A design concept for conduction cooling is presented.

A. Design requirements

In the following section we discuss the choice of wiggler parameters and technology required to achieve the ultra-low emittance. Both bending magnets and wiggler magnets contribute to the damping time and the emittances. A detailed general mathematical analysis of the dependence of the emittances and the damping times on the various parameters can be found in [7]. The concept and the list of the parameters for the CLIC damping rings can be found in [8, 9]. Three effects are determining the equilibrium emittance:

- Excitation and damping occurs due to the emission of synchrotron radiation. The damping is based on the effect that emission of synchrotron radiation reduces both the longitudinal and the transverse momentum of the electron. However, the cavities only restore the longitudinal momentum leading to a reduction of the transverse momentum. The equilibrium emittance calculated by considering these two effects is called zero-current emittance.
- Intrabeam scattering causes an increase of the zero-current emittance (determined by the effects mentioned above) due to small angle multiple Coulomb scattering.

The physical analysis of damping and excitation, without considering the effect of intrabeam scattering, allows the following conclusions to be drawn: in order to make the wiggler section as short as possible, the magnetic flux density B_w has to be large. Also the damping time τ is

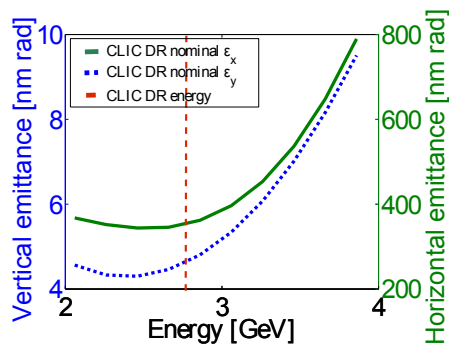


FIG. 5. Vertical and horizontal normalized emittances versus beam energy [3].

shorter the larger B_w is. But a high wiggler magnetic flux density B_w only produces low emittances when the product of $|B_w^3|$ and the period length λ_w^2 is small. Therefore, the ideal damping ring has wigglers with a large magnetic flux density B_w at a short period length λ_w .

However, the effective emittance in the ring will be larger than the zero-current emittance because of the effect of intrabeam scattering. The final normalized emittance of the beam $\gamma\epsilon_u$, with $u = x, y, z$ is given by:

$$\gamma\epsilon_u = \gamma\epsilon_{u,0} + \gamma\epsilon_{u,IBS}. \quad (1)$$

The normalized emittance growth from intrabeam scattering is proportional to the brightness of the beam, that is,

$$\gamma\epsilon_{u,IBS} \propto \frac{NQ}{\epsilon_x^{b_1} \epsilon_y^{b_2} \epsilon_z^{b_3}}, \quad (2)$$

where N is the number of particles per bunch and $\{Q, b_1, b_2, b_3\}$ is a set of positive real numbers. The effect of intrabeam scattering in existing rings is small, but in the first design studies [8] of the CLIC damping rings, the magnitude of the final emittance was dominated by intrabeam scattering. Therefore, in [3] the damping rings were re-optimized such that $\gamma\epsilon_x/\gamma\epsilon_{x,0} \leq 1.9$.

Fig. 5 shows the calculated emittance taking into account all the previously mentioned effects for beam energies between 2 and 4 GeV. The emittances have a broad minimum between 2 and 3 GeV. From Fig. 5, an energy of 2.86 GeV was chosen. A more detailed analysis can be found in [3].

In the next step, B_w and λ_w for the damping wigglers have to be specified. In Fig. 6 the area is marked where the horizontal, vertical, and longitudinal emittance requirements of the CLIC damping rings are met.

The maximum achievable flux density strength B_w as a function of the gap to period length ratio g/λ_w and the pole magnetic flux density B_p can be derived in free space from Maxwell's magneto-static equations:

$$B_w = \frac{B_p}{\cosh\left(\pi \frac{g}{\lambda_w}\right)}, \quad (3)$$

TABLE I. Parameters of wiggler magnet prototypes.

	Nb-Ti HR	Nb ₃ Sn VR
Short Sample		
B_w	3.6 T	5.5 T
max stored E	80 kJ	700 kJ
I_c at B_w	740 A	1250 A
B_s at B_w	6.3 T	9.9 T
Operational Parameters		
B_w^d	3.0 T	4.0 T
T_c^d	5.1 K	11.9 K
I^d	630 A	855 A
B_s^d	5.4 T	6.7 T
oper. T	4.2 K	4.2 K
gap	18 mm	18 mm
λ_w	56 mm	56 mm
K	15.7	20.9
Strand	Bochvar Institute [12]	OST RRP [13]

where B_p is the pole field on the iron (see Fig. 2).

The gap of superconducting wiggler magnets is determined by the required aperture and space to intercept the heat and radiation load from the beam. An aperture of 13 mm is foreseen in the damping rings. To intercept the heat and radiation load from the beam, 2.5 mm space on each side is required. Therefore, the magnetic gap was set to 18 mm for these calculations.

The normalized horizontal and vertical emittances have to be pre-damped from $100 \mu\text{m rad}$ for electrons and $9.7 \times 10^3 \mu\text{m rad}$ for positrons to $63 \mu\text{m rad}$ (horizontal) and $1.5 \mu\text{m rad}$ (vertical) in pre-damping rings [10]. For the emittance calculations the normalized vertical zero-current emittance was set to 4 nm rad, and the normalized longitudinal zero-current emittance was set to 6000 eV m. The total wiggler length in one ring was set to 104 m. Fig. 6 shows the results of this study. Fig. 6 (top) shows the normalized horizontal emittance as it is the most critical and can be used to decide on the required wiggler parameters. The red and the blue curves show the maximum achievable field for superconducting wiggler magnets with Nb₃Sn and Nb-Ti wire technology, respectively. The red and the blue points present the proposed Nb₃Sn and Nb-Ti working points. The parameters of the wiggler magnets represented by these points are presented in Tab. I. Fig. 6 (bottom) presents the effect of intrabeam scattering (IBS) on the normalized emittance, for example a value of 1.2 means that 20% of the emittance is generated by the effect of IBS.

Fig. 6 (top) shows that only wigglers with a period length λ_w of less than 80 mm and with a sinusoidal wiggler field with a magnetic flux density amplitude B_w larger than 2.2-2.5 T fulfill the requirements of the CLIC damping rings. For period lengths λ_w of 50 to 80 mm and magnetic flux densities B_w of 2.8-4.5 T the effect of intrabeam scattering (Fig. 6 (bottom)) can be minimized.

In the prototype phase the wiggler magnets will be tested in the ANKA storage ring and will also be used as a light source. Therefore, a smaller period length

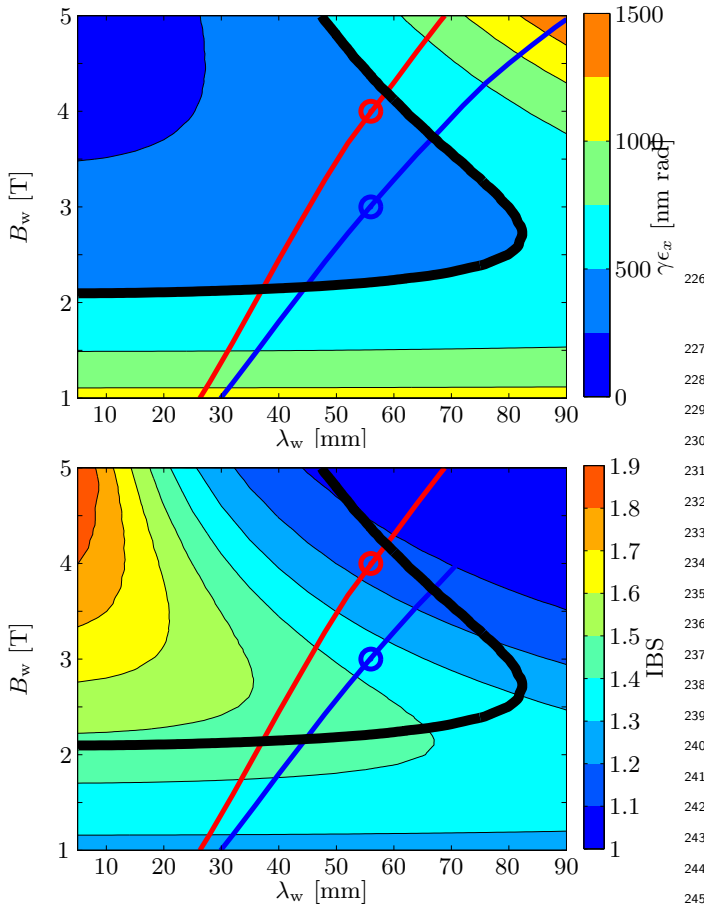


FIG. 6. Equilibrium normalized horizontal emittance $\gamma\epsilon_x$ (top) and the effect of IBS ($\gamma\epsilon_x/\gamma\epsilon_{x,0}$). The red and the blue curves show the maximum achievable magnetic flux density for superconducting wiggler magnets with Nb₃Sn and Nb-Ti wire technology, respectively.

208 λ_w was chosen to satisfy the needs of both ANKA and
 209 CLIC. The Nb-Ti wiggler magnet will be operated with
 210 a loadline margin of 85% and the Nb₃Sn wiggler mag-
 211 net with a loadline margin of 68%. The loadline margin
 212 for Nb₃Sn was chosen larger for additional margin be-
 213 cause the manufacturing and operation of Nb₃Sn wiggler
 214 magnets is purely R&D. Each of the 104 superconduct-
 215 ing wiggler magnets has 34 periods. 26 wigglers will be
 216 installed in each of the straight sections of the two damp-
 217 ing rings. This discussion shows that the development
 218 of short-period superconducting wiggler magnets with a
 219 high magnetic flux density strength B_w and small gap g
 220 is required.

221 Hybrid-permanent wiggler magnets are not able to
 222 reach the required large magnetic flux densities. The
 223 magnetic saturation induction of iron ($B = 2.15$ T) can
 224 be considered as the theoretical upper limit for the pole
 225 field of hybrid-permanent magnet wigglers.

TABLE II. Nomenclature.

B_w^*	Maximum achievable field at λ_w
$B_p^*, B_s^*, I_c^*, J_{eng}^*$	Corresponding values at B_w^*
$B_p^d, B_s^d, I^d, g^d, \lambda_w^d$	Design operating values

II. WIGGLER MAGNET DESIGN

227 In this section we present a conceptual design for su-
 228 perconducting wiggler magnets. From the requirements
 229 of the CLIC damping rings, the gap size g , the period
 230 length λ_w and the minimal required magnetic flux den-
 231 sity in the center of the gap B_w are assumed to be given.
 232 The choice of the wiggler coil design, the choice of the
 233 strand technology (Nb-Ti or Nb₃Sn) and the choice of
 234 the wire bundle dimension are discussed in the follow-
 235 ing. Further on, in the case of vertical wiggler magnets,
 236 the bending radii of the end-coils have to be determined.
 237 The parameters required for the optimization are sum-
 238 marized in Tab. II and illustrated in Fig. 2, where B_w
 239 refers to the amplitude of the magnetic flux density, B_p
 240 to the pole field and B_s to the surface field on the conduc-
 241 tor. We chose not to investigate the graded coils (coils
 242 with changing engineering current density over the wire
 243 bundle) because they require the use of multiple power
 244 supplies and current leads. All magnetic calculation were
 245 performed by using the Opera software package [11].

246 We assume that the design parameters B_w^d, λ_w^d and
 247 g^d are given; the design pole field B_p^d can be directly
 248 calculated by using

$$B_p^d = B_w^d \cosh \pi \frac{g^d}{\lambda_w^d}. \quad (4)$$

249 Fig. 7 (top) can be used to find the required engineering
 250 current density J_{eng}^* from the intersection of $B_p^d = B_p^*$
 251 and the design period length $\lambda_w^d = \lambda_w$, where $*$ denotes
 252 the maximum achievable pole field B_p^* for a period length
 253 λ_w at the engineering current density J_{eng}^* . In this first
 254 step of the optimization, the design pole field B_p^d is set
 255 to the maximum achievable pole field B_p^* for a given pe-
 256 riod length λ_w at the engineering current density J_{eng}^* .
 257 In Fig. 7 a gap of 18 mm was assumed, which can be
 258 adjusted by using Equation (4).

259 After determining the required engineering current
 260 density J_{eng}^* for the desired pole field in Fig. 7 (top),
 261 $B_p^d = B_p^*$; the maximum field on the conductor B_s^* can
 262 be read off from the intersection of J_{eng}^* and the period
 263 length λ_w in Fig. 7 (bottom). If the intersection point of
 264 J_{eng}^* and the period length λ_w^* are below the critical sur-
 265 face shown for Nb-Ti (Bochvar Strand) or Nb₃Sn (OST
 266 RRP) it can be, in principle, realized.

267 If a strand is used that is different from the two shown
 268 in Fig. 7 the engineering current density has to be con-
 269 verted correspondingly into the current in the strand with

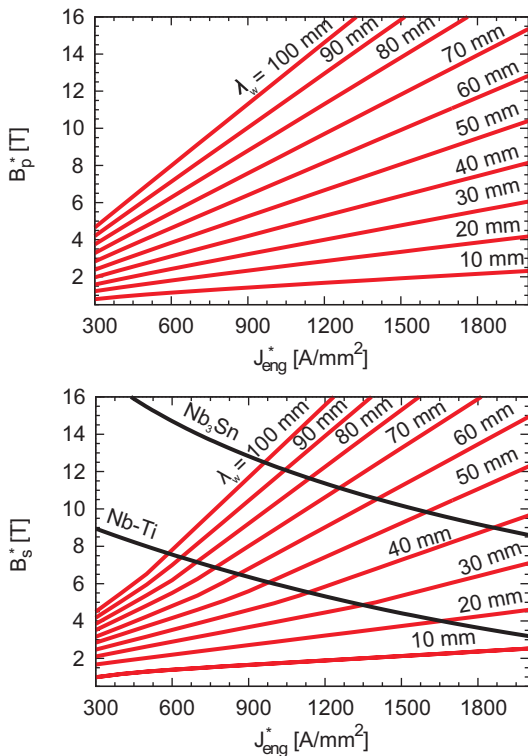


FIG. 7. Top: Optimized field at the pole tip B_p^* versus engineering current density. Bottom: Load lines for wiggler magnets with a coil width ($0.3\lambda_w = y_c = z_c$) and a gap 18 mm. For example, in the bottom plot, we find that an engineering current density $J_{\text{eng}}^* = 975 \text{ A/mm}^2$ yields a maximum surface field $B_s^* = 6 \text{ T}$ for a Nb-Ti strand at a period length $\lambda_w = 50 \text{ mm}$. The top plot shows that this wiggler configuration would yield a maximum pole field $B_p^* = 5.5 \text{ T}$.

270

$$I = \frac{1}{\kappa} J_{\text{eng}}, \quad (5)$$

where we define the filling factor κ for the wiggler magnets as the average number of wires per unit area. For the calculations presented here, a filling factor of 1.24 strands/ mm^2 was assumed. As Fig. 7 reveals, $B_p \propto J_{\text{eng}}$. Therefore, the part of the coil generating the field seen by the beam must be densely wound. In vertical wiggler magnets, the layer jump can be conveniently placed on the side averted from the beam. In horizontal racetrack coils, usually the layer jump is placed in the straight part, resulting in an around 10% smaller filling factor compared to that of vertical wiggler magnets.

We have to introduce the critical surface in order to determine if the chosen strand is superconducting at the chosen B_s (shown for the two sample strands in black in Fig. 7 (bottom)). A superconducting filament in a magnetic field is superconducting as long as the current is smaller than the critical current. For a Nb-Ti strand, the critical current is [14]

$$I_c = C B_s^{\alpha-1} \left(1 - \frac{B_s}{B_{c2}(T)} \right)^\beta. \quad (6)$$

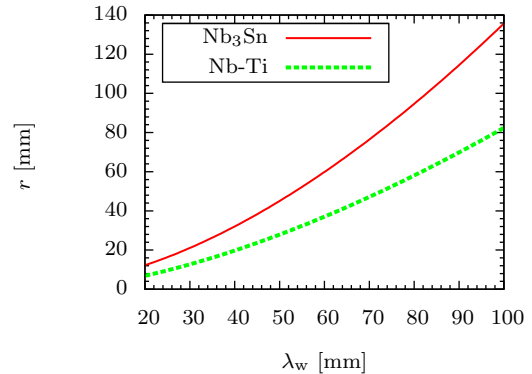


FIG. 8. Optimized end-coil radius r for Nb-Ti and Nb₃Sn wiggler magnets with zero force in the end-coil.

For the Nb-Ti Bochvar Institute strand, $C = 3300$, $\alpha = 0.72$, $\beta = 1.1$, and $B_{c2}(4.2) = 10.68$. For a Nb₃Sn strand, the critical current is [15, 16]

$$I_c = \frac{C}{\sqrt{B_s}} \left(1 - \frac{B_s}{B_{c2}(T, \epsilon)} \right)^2. \quad (7)$$

For the OST RRP 0.8mm strand, $C = 11030$, $B_{c2}(4.2, 0) = 24.92$.

In vertical racetrack wigglers, the bending radius can be chosen at will. It is useful to choose it in a way that the Lorentz force acting on the wire bundle is compressive. Fig. 8 shows the bending radii for Nb-Ti and Nb₃Sn wiggler magnets at which the force becomes zero. For larger bending radii, the Lorentz force is compressive; for smaller bending radii, the Lorentz force is tensile. In horizontal racetrack wiggler magnets this option obviously does not exist because the bending radii are given by the pole width. Because the pole width is much smaller than the radii shown in Fig. 8, the Lorentz forces in the end-coils of horizontal wiggler magnets are tensile. In the straight section, the wire bundles are compressed towards the unsaturated iron. If no iron is used, the forces will be tensile. A yoke on top of a vertical wiggler magnet reduces the resulting force on the wire bundles on the upper straight part. One has to be careful at the first and last coils of the wiggler magnets. Forces acting away from the wiggler body occur and have to be supported by an adequate mechanical structure.

Wiggler magnets have to be transparent for the beam. That means, the first and second field integrals

$$I_y = \int_{s_0}^{s_1} B_y(z) dz, \quad (8)$$

$$II_y = \int_{s_0}^{s_1} \int_{s_0}^s B_y(z') dz' dz, \quad (9)$$

over the wiggler magnet have to vanish. Two different designs are commonly used to compensate the first and second field integral, either a symmetric (odd number of poles) or an antisymmetric (even number of poles) design. In superconducting wiggler magnets the antisymmetric

321 design is preferred. The first field integral automatically
 322 becomes zero and reduces the possibility of beam trips
 323 in the case of a quench [17]. Further, the integrals of
 324 the higher even multipoles (sextupole, decapole, ...) are
 325 canceled automatically because they are equal in size but
 326 different in sign. The second field integral has to be min-
 327 imized by varying the number of conductors or the ge-
 328 ometry of the last coils by using a numerical calculation
 329 method. If the magnet is operated at different current
 330 levels, the first and last pole should be thick enough to
 331 not saturate.

332 In the last paragraph, we saw that all even multi-
 333 poles are canceled automatically. Finally we have to
 334 ensure that the influence of the odd numbered multi-
 335 poles (quadrupoles, octupoles,...) remains also accept-
 336 ably small. Tolerances for the dynamic field integral
 337 $\int B_y ds$ have to be determined by performing tracking
 338 studies to specify the allowable range, where s denotes
 339 the trajectory of the particles. It is shown in [18] that
 340 it is not sufficient to consider $\int B_y dz$, where z follows
 341 the global coordinate of the overall beam direction. The
 342 good-field region is defined as the region where the rela-
 343 tive change in magnetic flux density is less than 1×10^{-4} .
 344 Fig. 9 shows this region for typical wiggler designs. The
 345 maximum deflection of the beam in a wiggler magnet in
 346 the CLIC damping rings is $x = 2.65 \times 10^{-3} B_w \lambda_w^2$, where
 347 all values have to be entered in SI units. For $B_w = 3$ T
 348 we find around $\pm 30 \mu\text{m}$. The beam size is smaller than
 349 1.2 mm. We suggest to choose a good-field region of at
 350 least 4 mm.

351 The final step in the magnet design of a superconduct-
 352 ing wiggler is the quench analysis. A quench is a transi-
 353 tion from the superconducting to the normal-conducting
 354 state followed by a thermal runaway. When the super-
 355 conductor becomes normal conducting, the current flows
 356 through the stabilizing copper of the strand causing resis-
 357 tive heating of the magnet, which has to be switched
 358 off. Wigglers can be built and protected in modules; in
 359 the extreme each half period can be protected separately
 360 by means of a parallel resistor within the magnet cold-
 361 mass, as was done for the LHC beam diagnostics undu-
 362 lator [19]. If a coil of the wiggler quenches, the parallel
 363 resistor acts both as energy extraction for the quenched
 364 coil and by-pass for the current. This protection scheme
 365 is feasible because the stored energy in a single coil of
 366 a wiggler magnet is relatively small (< 10 kJ). A PSpice
 367 simulation was performed. As input parameter the resis-
 368 tance increase value after the occurrence of a quench
 369 was extrapolated from the CERN-KIT short model wig-
 370 gler (Section III). The analysis has shown that even the
 371 protection of many wiggler magnets powered in series is
 372 feasible.

373 A. Influence of field errors

374 Magic fingers magnetic shims can be used to compen-
 375 sate both for small errors of the first and second field

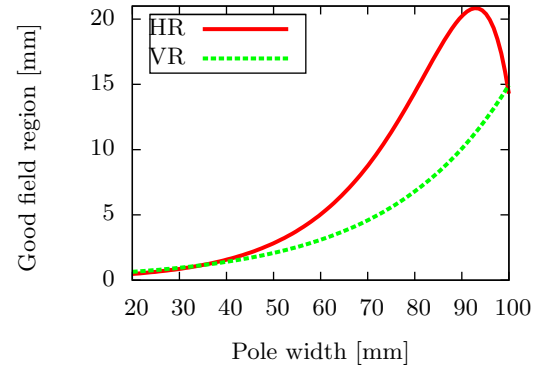


FIG. 9. Example of rolloff of wiggler magnets ($\lambda_w = 56$ mm).

376 integrals and for small multi-pole errors due to mechani-
 377 cal errors in the wiggler magnets [18]. Additional steerers
 378 can be used for compensation of the field integrals.

379 The horizontal equilibrium emittance and the damping
 380 time [7] without considering the effect of intrabeam scat-
 381 tering vary less than 5% over a hypothetical, one million
 382 damping rings with Gaussian distributed errors of the
 383 magnetic flux density amplitude B_w and period length
 384 λ_w . The standard deviation for this study was set to:
 385 $\sigma(B_w) = 0.2$ T and $\sigma(\lambda_w) = 1$ mm. A standard devia-
 386 tion of $\sigma(B_w) = 0.2$ T corresponds to an error in the pole
 387 height of ± 1.5 mm if $B_p = \text{const}$ and $\lambda_w = \text{const}$. These
 388 tolerances can be easily achieved. Therefore, no special
 389 care has to be taken to maintain small tolerances during
 390 the manufacturing of the wiggler magnets.

391 Notice that if the yaw, pitch, or roll angles obtained
 392 with magnet alignment do not meet the target values,
 393 higher-order field components are introduced which are
 394 not represented in the field model described above.

395 B. Temperature level of SC coils

396 The operation at 1.9 K instead of 4.3 K increases the
 397 performance of a Nb-Ti wiggler by around 20% ($\lambda_w =$
 398 56 mm). However, a Nb₃Sn wiggler with currently tested
 399 strands reaches almost the same B_w at 4.3 K and 1.9 K
 400 due to self-field instabilities. Only the latest Nb₃Sn
 401 strand development may reach larger currents at 1.9 K
 402 [20]. Cooling at around 4.2 K can be economically pro-
 403 vided by standard cryocoolers. Therefore, cooling at
 404 1.9 K is not pursued. The power consumption at 1.9 K
 405 would be above 200 kW instead of 76.9 kW and could not
 406 be provided by cryocoolers (Section IV).

407 The wire bundle shown in Fig. 2 is encased in epoxy
 408 resin. Therefore, the superfluid helium cannot come in
 409 direct contact with the superconducting wire. As a result
 410 the large thermal conductivity of superfluid helium at
 411 1.9 K is only of limited advantage. Therefore, we choose
 412 to operate the wiggler magnets at 4.2 K, which eases cool-
 413 ing considerably and allows for cooling the wiggler mag-
 414 nets with cryocoolers.

TABLE III. Parameters of short models.

	CERN-KIT	CERN-BINP
Period, mm	40	50
Stored Energy, kJ	1	10
Gap, mm	16	20
B_w , T at 4.2 K	1.9	2.2
B_w , T at 1.9 K	2.4	—
I_c at 4.2 K, A	730	700
B_s at 4.2 K, T	4.8	6.5
I_c at 1.9 K	910	—
Cu/Sc ratio	1.8/1	1/1.5
# poles	6	8
Strand	LHC #3 [22]	Bochvar Institute [12]

III. CONCEPTUAL DESIGN VERIFICATION

Two Nb-Ti vertical racetrack short-models were successfully manufactured and tested in two independent collaborations. In the framework of the CERN collaboration with the Karlsruhe Institute of Technology (KIT), Germany, a 40 mm period, Nb-Ti short-model was manufactured reaching up to 2.4 T at 1.9 K. The magnet reached short sample current after 13 quenches. The results are published in [21]. In the framework of the CERN-Budker Institute of Nuclear Physics (BINP), Russia, collaboration, Nb-Ti short-models with a period length of 50 mm were manufactured reaching up to 2.2 T at 4.2 K. The magnet reached short sample current after 20 quenches. The parameters of the two successfully tested short models are summarized in Tab. III. These tests have proven that Nb-Ti wiggler magnets in the proposed parameter space can be manufactured and operated.

IV. THERMAL DESIGN

This section presents a thermal design for the CLIC damping wigglers. It will be the first time that 26 superconducting wiggler magnets will be operated in one straight section. In this chapter we address the challenges related to this operation mode. For all following calculations the baseline parameters were used. The wiggler baseline design is the Nb-Ti HR design presented in Tab. I (left column). The baseline energy of the CLIC damping rings is 2.86 GeV.

A. Magnetically and electrically induced heat loads

Eddy currents will occur due to the varying magnetic flux density during the ramp-up or a quench of the wiggler magnets. For the test device in ANKA the ramping time is crucial, because during injection the wiggler has to be shut down. Therefore, the test device will be built

TABLE IV. Comparison of different joint technologies [23, 24].

	Electrolytic Cu	Soldered	US welded	Cold welding
Nb-Ti	20 nΩ cm	40 nΩ cm	8 nΩ cm	< 1 pΩ cm
Nb ₃ Sn	20 nΩ cm	40 nΩ cm	-	< 10 nΩ cm

by using laminated iron to minimize eddy currents during the ramp-up.

Resistive joints cannot be avoided. The horizontal racetrack wiggler magnets will have around 75 joints per meter wiggler length. Tab. IV summarizes the achieved resistance values normalized to a 1-cm overlap length. Cold welded Nb-Ti filaments joints lead to the smallest resistances:

$$\frac{P}{L} < \frac{nRI^2}{L} < 1 \frac{\text{mW}}{\text{m}}, \quad (10)$$

where P is the power, L the length of the wiggler, n the number of joints, R the resistance of one joint, and I the current in the strand. In the case of vertical racetrack wiggler magnets, the only joints are the interconnections to the current leads. This would yield for 4 interconnections operated at 855 A approximately 15 mW heat load.

B. Beam induced heat loads

1. Image currents

In [25] the anomalous skin effect was measured for metals with a small resistance at high frequencies. In this regime Ohm's law can no longer be applied because the free path of the conduction electrons is similar to the penetration depth of the electric field [26].

At cryogenic temperatures the electrical resistivity of pure metals such as OFHC copper is up to a factor of 300 lower than at room-temperature. Therefore, the average power deposition per unit length due to the wakefield of the beam in the extreme anomalous skin effect regime of a cold beam pipe for aluminum or copper (coating) is given by [27]:

$$P/L = \frac{\Gamma(\frac{5}{6})cZ_0}{4b\pi^2} \frac{I_{av}^2}{\sigma_z^{\frac{5}{3}}\eta f_{RF}} B_{Mat} \approx 1 \frac{\text{W}}{\text{m}}. \quad (11)$$

The presented values for the image current power deposition were calculated with the values defined and given in Tab. V.

While good conductors do enter the anomalous skin effect regime at cryogenic temperatures and high frequencies, poor conductors do not. For poor conductors such as uncoated stainless steel or TiZrV ternary alloy, called Non Evaporable Getter (NEG) coating, the heat load can be estimated by normal skin effect formulas:

$$P/L = \frac{\Gamma(\frac{3}{4})c\sqrt{Z_0}}{\sqrt{32}b\pi^2} \frac{I_{av}^2}{\sigma_z^{\frac{3}{2}}\eta f_{RF}} \frac{1}{\sqrt{\sigma_c}} \gtrsim 32 \frac{\text{W}}{\text{m}}. \quad (12)$$

TABLE V. Parameters for image current calculations, see Equations (11) and (12); parameter values from [9, 27].

Parameter	Value	Unit	Explanation
$\Gamma(\frac{5}{6})$	1.13		Gamma-function
B_{Al}	3.3×10^{-7}	$m^{\frac{2}{3}}$	Material constant, Al
B_{Cu}	3.9×10^{-7}	$m^{\frac{2}{3}}$	Material constant, Cu
σ_c	2×10^6	Sm^{-1}	St. steel conductivity (4.3 K)
Z_0	120π	Ω	Free space impedance
c	3×10^8	$\frac{m}{s}$	Speed of light
I_{av}	0.15	A	Average current
b	5.5×10^{-3}	m	Beam pipe radius (reduced)
σ_z	1.4×10^{-3}	m	Bunch length
ηf_{RF}	$0.22 \times 1 \times 10^9$	Hz	Fraction of the ring circumference occupied by a bunch train for 1 GHz
	312		Number of bunches (2 trains \times 156 bunches)
	4.1×10^9		Bunch population
	420	m	Ring circumference
	1.4×10^{-6}	s	Orbital period
	10^{-9}	s	Bunch separation

486 A material with poor conductivity is not acceptable be-
 487 cause of its high heat load. Therefore, all the following
 488 calculations assume a high-conductivity material for the
 489 beam pipe.

490 2. Electron clouds

491 The heat load estimation due to electron clouds in the
 492 electron and positron damping rings were performed with
 493 the ECLOUD code [28]. Fig. 10 (top) shows the heat load
 494 induced by electron clouds in the electron damping ring.
 495 Multipacting is a phenomenon of resonant electron multi-
 496 plication in which a large number of electrons is built up,
 497 leading to remarkable power losses, heating of the beam
 498 pipe and beam instabilities [29]. The electron beam is
 499 not affected by multipacting for values of a secondary
 500 electron emission yield δ_{max} up to 2.4.

501 In the positron ring, multipacting appears for a sec-
 502 ondary electron emission yield $\delta_{max} > 1.3$ and causes
 503 significantly stronger e-cloud effects over one train pas-
 504 sage for values above 1.4–1.5; see Fig. 10 (bottom). As
 505 electron clouds cause not only heat load but also beam in-
 506 stabilities, low secondary electron emission yield coating
 507 is needed for the positron damping ring. The needs for
 508 the beam-pipe coating to avoid heating from e-clouds and
 509 from image currents are contradictory, because a large
 510 electron emission yield means usually a low resistivity of
 511 the beam-pipe coating. A thin-film low-secondary-yield
 512 coating may be sufficient to reduce the secondary elec-
 513 tron emission, such a thin-film coating may not decrease
 514 the beam pipe conductivity; surface treated grooved cop-
 515 per or amorphous carbon might be another solutions [30].
 516 The effect of e-cloud at low emittance rings is studied in
 517 detail at CsrTA [31].

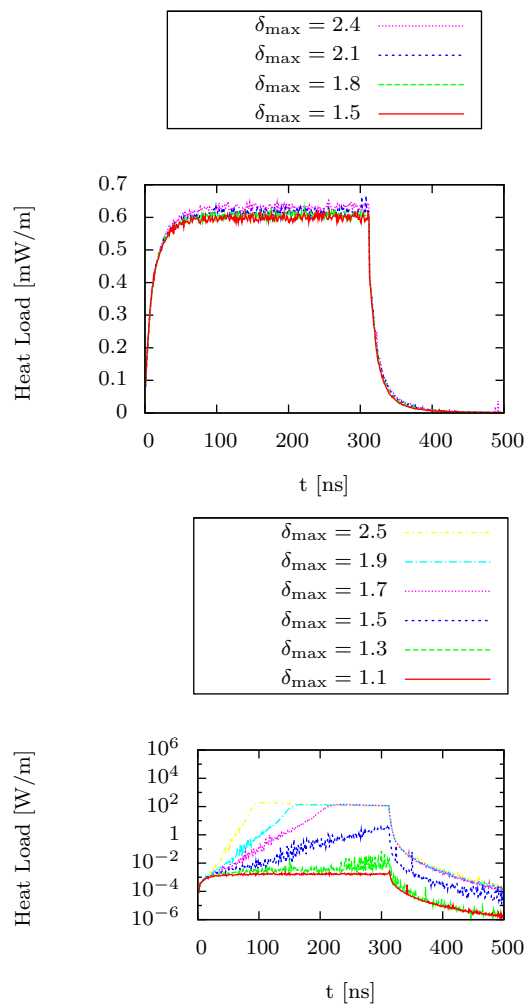


FIG. 10. Heat load induced by electron clouds in the electron damping ring (top). Heat load induced by electron clouds in the positron damping ring (bottom).

518 3. Synchrotron radiation

519 Most synchrotron radiation generated in the damping
 520 wigglers has to be absorbed at ambient temperature to
 521 avoid heating of the superconducting coils. Fig. 11 shows
 522 the principle of synchrotron radiation emission and ab-
 523 sorption. The radiating charged particle is moving on
 524 a sinusoidal trajectory in the horizontal xz -plane. The
 525 angles of observation in horizontal and vertical direc-
 526 tions are θ and ψ . The emitted light, which will not
 527 be absorbed by up-stream absorbers (yz -plane), shown in
 528 cones, will partly irradiate the beam pipe. As an example
 529 ψ_3^{max} is shown, the maximum angle at which wiggler W3
 530 can irradiate synchrotron radiation on the beam-pipe.
 531 The heat load on the beam pipe is calculated on nodes,
 532 which are equidistantly spaced. In this example only the
 533 synchrotron radiation of the two last wigglers can hit the
 534 beam pipe. Rectangular absorbers are proposed, because
 535 of manufacturing constraints. The power emitted from
 536 wiggler magnets is mainly concentrated within a light-

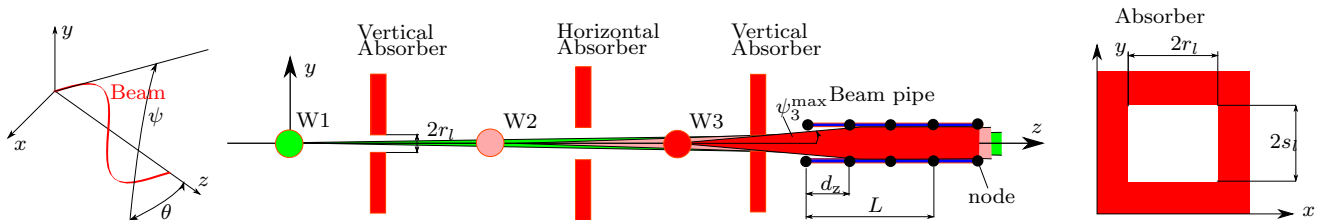


FIG. 11. Principle of synchrotron radiation emission (left), absorber scheme (middle), and absorber layout (right).

TABLE VI. Heat load on last wiggler beam pipe after a horizontal absorber for different wiggler lengths L .

L , m	1	2	3	4	5	6
P , W	7	40	120	280	560	980

TABLE VII. Lattice for heat load calculation of synchrotron radiation.

Element	Length, m	$2s_l$, mm	$2r_l$, mm	Shape
Horizontal absorber				
Wiggler	2	13	80	Elliptical
Transition and quadrupole	0.25	13	80	Elliptical
Absorber	0.5	13.5	12.3	Rect.
Transition	0.25	13	40	Elliptical
Vertical absorber				
Wiggler	2	13	80	Elliptical
Transition and quadrupole	0.25	13.5	40	Elliptical
Absorber	0.5	9.5	12.5	Rect.
Transition	0.25	13.5	40	Elliptical
Beam pipe (heat load)	2	13	80	Elliptical

cone of small opening angle $K/\gamma \approx 3$ mrad, where K is the wiggler's deflection parameter and γ is the relative energy. However, the distance between the first wiggler and the last wiggler is around 80 m, which implies that a large part of the generated synchrotron radiation would irradiate the beam pipes of the up-stream superconducting wigglers. A detailed mathematical description of the calculation method is given in Appendix A.

The heat load depends on the distance between the absorbers and therefore on the wiggler length (Tab. VI). From Tab. VI results the choice of two meter long wiggler magnets, because the heat load from synchrotron radiation increases rapidly. Shorter wiggler magnets are not chosen, because each cryostat requires an approximately two times 0.5 m long cold-warm transition which reduces the compactness of the ring. The corresponding lattice design is presented in Tab. VII.

Fig. 12 shows the heat load distribution on the beam pipe of the two last installed wiggler magnets (number 25 and 26) downstream of absorbers installed after quadrupoles aligned with their focusing planes. The horizontal aperture of the wiggler has to be large enough to reduce the heat load from synchrotron radiation (Tab. VIII). Fig. 13 shows the contribution of each wiggler to the total heat load on the last and next-to-last wigglers. The total heat load from synchrotron radiation

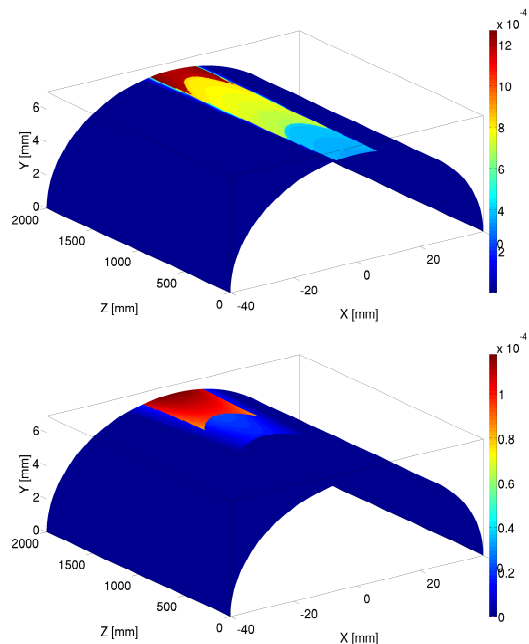


FIG. 12. Spatial distribution of synchrotron radiation on the beam pipe for the 25th wiggler with a total heat load of 40 W (top) and the 26th wiggler with a total heat load of 2 W (bottom) for the Nb-Ti baseline design (Units in Figure: W/mm²).

TABLE VIII. Heat load on the 25th beam pipe for different horizontal apertures (widths).

Width, mm	30	40	50	60	70	80
Heat load, W	62.8	47.9	43.1	40.9	39.6	38.9

on the beam pipe downstream of a vertical absorber is less than 2 W and around 40 W downstream of a horizontal absorber. The first six wiggler magnets in the straight section of the damping rings are subject to less heat load.

4. Absorption of synchrotron radiation in the beam pipe

The critical photon energy ϵ_c of the CLIC damping wiggler can be calculated according to [32]:

$$\{\epsilon_c\}_{\text{keV}} = 0.665 \{E\}_{\text{GeV}}^2 \{B_w\}_T \approx 16 \text{ keV}. \quad (13)$$

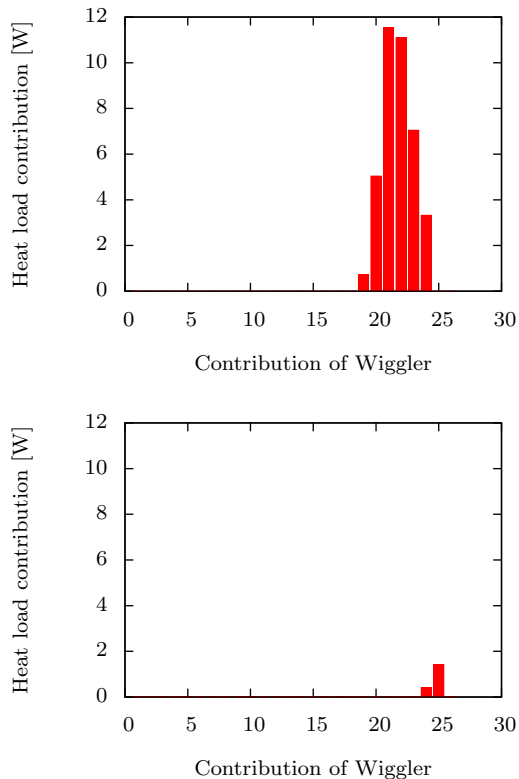


FIG. 13. Heat load on the 25th and 26th beam pipe of the wiggler magnets due to synchrotron radiation from upstream wiggler magnets.

570 The spectral intensity decreases rapidly for photon energies above ϵ_c .

572 The measured intensity I transmitted through a layer
573 of material with thickness l is related to the initial intensity I_0 according to the Beer-Lambert law [33]:

$$\frac{I(l)}{I_0} = e^{-\mu l}, \quad (14)$$

575 where l denotes the penetration depth. The attenuation
576 coefficient is μ . If we limit the transmitted energy
577 to 1% of the initial intensity, the penetration depth can
578 be calculated by $l_{1\%} = 4.6 \frac{1}{\mu}$. For a photon energy of
579 $3\epsilon_c \approx 50$ keV, the attenuation coefficients for common
580 beam pipe materials and the corresponding penetration
581 depths are given in Tab. IX. The maximum penetra-
582 tion depth l_{\max} at the full radiation cone opening angle,
583 shown in Fig. 14, is also given in Tab. IX. It was as-
584 sumed that the synchrotron radiation changes the angle
585 to the beam axis when entering the vacuum chamber by
586 Snell's law. In the following it was assumed that this an-
587 gle changes by a factor of 5. The maximum penetration
588 depth is much smaller than the material thickness of the
589 beam pipe (1 mm). Therefore, all synchrotron radiation
590 will be absorbed in the inner part of the beam pipe and
591 no heat will be deposited directly into the superconduct-
592 ing coils.

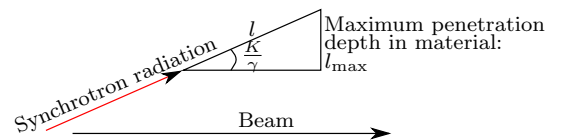


FIG. 14. Maximum penetration depth l_{\max} of synchrotron radiation depending on the maximum opening angle of the radiation cone.

TABLE IX. Attenuation coefficients, densities and penetration depths for a photon energy of 5×10^{-2} MeV [33].

Material	$\mu/\rho, \text{cm}^2 \text{g}^{-1}$	$\rho, \text{g cm}^{-3}$	μ, cm^{-1}	l, cm	$l_{\max}, \mu\text{m}$
Al	0.3681	2.699	0.994	4.628	454
Cu	2.613	8.960	23.41	0.1965	19
Fe	1.958	7.874	15.42	0.298	29

593

5. Absorber heat load

594 The absorber design was optimized such that the heat
595 load on the vertical and horizontal absorbers is approx-
596 imately balanced and reaches, after some 5 to 10 ab-
597 sorbers, its maximum value. Fig. 11 shows the principle
598 layout of the absorbers. They will be water-cooled. After
599 the last wiggler magnet a dump will be installed to ab-
600 sorb the remaining synchrotron radiation. Fig. 15 shows
601 the heat load on each of the 26 absorbers.

602 A detailed mathematical description of the calculation
603 method is given in Appendix B.

604

C. Cooling concept and related heat loads

605 Fig. 16 compares the standard cooling concept (bath
606 cooling, left) with the cooling concept for the CLIC
607 damping wigglers proposed in the introduction (indirect
608 cooling, right and Fig. 3). For indirect cooling the whole
609 wiggler magnet is in an insulation vacuum. The he-
610 lium is contained in the heat exchangers. In bath cool-

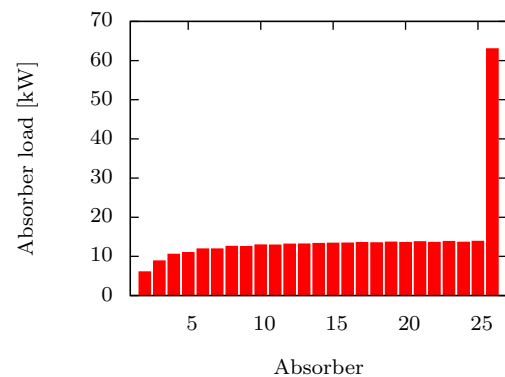


FIG. 15. Absorber load distribution including the dump at the end of the straight section.

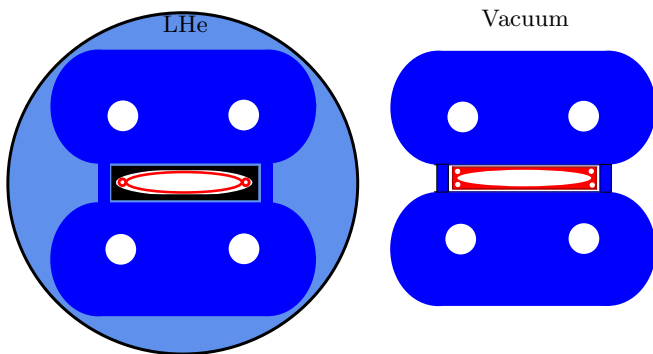


FIG. 16. Two cooling concepts. Left: Bath cooling. The magnet is immersed in liquid helium (LHe). Right: Indirect cooling. The whole wiggler magnet is in vacuum. The helium is contained in the heat exchangers.

ing the magnet is immersed in liquid helium (LHe). To extract the heat a copper liner cooled with gaseous helium contained in heat exchangers is required (depicted in red). Further, a mechanically stable pipe that can withstand the pressure increase during a quench (in black) is needed. This pipe also insulates the beam vacuum from the surrounding liquid helium. Although indirect cooling requires a detailed thermal design of the superconducting coils it comes with a number of advantages compared to bath cooling:

- Mechanically less demanding beam pipe. Bath cooling would require a stainless steel beam pipe to sustain the pressure increase during a quench. Without this requirement a 2 mm smaller gap can be realized, resulting in a more than 10% higher gap-field B_w .
- Less complex cryogenic structure because all helium is contained within the heat exchangers resulting in smaller helium mass, smaller valves, tubes, etc.
- Cryostat design for exchangeable coils and vacuum pipes for maintenance and repairs is less complex.

An insulating vacuum of 10^{-4} Pa will be established to minimize the heat transfer to the superconducting coils by convection. The superconducting coils and the beam pipe will be mounted with minimal thermal contact and with materials such as glass-fiber reinforced plastics or kevlar stripes with a large strength to heat conductivity ratio. All surfaces should be wrapped with polished well-conducting metal foils or aluminized Mylar foils with small emissivities to reduce heat transfer by radiation.

The temperature of the beam pipe will be stabilized at around 20 K where the heat conductivity k of copper is highest (Fig. 17) resulting in an iso-thermal beam pipe. Cryocoolers for this temperature level are available, and radiation to the superconducting coils is kept to a minimum.

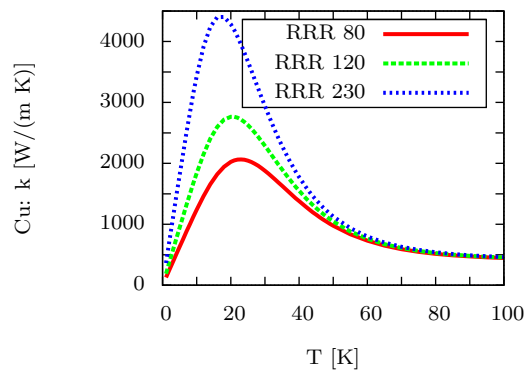


FIG. 17. Heat conductivity of OFHC copper versus temperature. Data from [39].

TABLE X. Summary of the average heat loads (all sources) at the different temperature levels in Watts.

	Shield 80 K	Beam pipe 20 K	SC coils 4.2 K
Synchrotron radiation (HA)		40.0	
Synchrotron radiation (VA)		2.0	
Average SR		21.0	
Image currents		2.0	
E-Clouds		0.02	
Radiation	16.3		0
Convection	1.0		0.10
Conduction	0.9		0.64
Joints	-		0.02
Current leads	72.0		0.16
Total (Average)	90.2	23.0	0.9

The heat load is deposited in the center of the cross-section of the 2 m long beam pipe (Fig. 12) and has to be transported over $\lesssim 50$ mm to the outer side of the beam pipe. The resulting temperature difference is smaller than $\Delta T < \frac{1}{2} \frac{\dot{Q}l}{kA} \approx 0.3$ K, with the heat load $\dot{Q} = 50$ W, the distance from the center of the beam-pipe to the heat exchanger $l = 50$ mm, the averaged heat conductivity $k = 2000$ W(m K) $^{-1}$ (RRR = 80), and cross-section $A \geq 2 \times 10^{-3}$ m 2 .

An overview of heat leak calculation methods for cryostats is given in [34–38]. The coils are in an insulation vacuum; therefore, the total heat load on the coils results mainly from conduction (current leads, and fixing structure) and is less than 1 W. Radiation and convection can be minimized by using a 60 to 80 K shield. No heat load induced by the beam is deposited directly into the coils because all heat load can be intercepted by a metallic beam pipe of a thickness of about 0.5 mm. The beam pipe can be cooled at a higher temperature level (20 K), which greatly reduces the consumed power for cooling. Tab. X gives a summary of all heat load sources occurring in the CLIC damping wigglers at the different temperature levels.

TABLE XI. Power consumption of the cryogenic plants at the different temperature levels. The total power consumption is around 450 kW.

Temperature Level, K	80	20	4.2
Total heat load, kW	11.3	2.9	0.113
Carnot Efficiency, %	33.3	6.7	1.3
Cryoplant Efficiency, %	23.0	19.3	11.3
Total Power Consumption, kW	147.5	224.3	76.9

D. Large scale cooling concept and power consumption

A total of 104 wiggler systems is needed for the two CLIC damping rings. Two cooling schemes are investigated: (1) A large scale cryogenic system connected to all wiggler magnets with cryogenic transfer lines. (2) Each wiggler magnet is independently cooled with small cryocoolers. In recent years cryocoolers have shown a considerable increase in performance, reliability and a dramatic decrease in costs.

The efficiency of large cryogenic plants can be calculated according to the Carnot efficiency [40] and with efficiency data of large-scale cryogenic plants taken from [41]. These data are in good agreement with more recent CERN experience (for example [42]):

$$P(T_{\text{op}}) \approx \frac{T_{\text{op}} - 1}{\alpha C^{\beta} - \gamma} C, \quad (15)$$

where $T_{\text{op}} = 320$ K, $C = [10, \dots, 10^6]$ W is the capacity of the cryoplant and $T = [4.2, \dots, 80]$ K the operating temperature of the cryoplant. The fitting parameters are: $\alpha = 35.7$, $\beta = 0.05$, and $\gamma = 33.9$.

Tab. XI presents the expected power consumption of the two rings with large scale cryogenic plants. Losses in the transfer-line can be kept small, for a well-shielded line 0.05 W/m [43]. In this calculation the losses of the distribution system were considered by adding 20% to the total required heat budget.

As an alternative to a large scale cryogenic plant, three different cryocoolers per wiggler with a total input power of around 24 kW [44], yielding a total power consumption of around 2.5 MW for the two damping rings are proposed.

Large scale cryogenic plants are favorable in terms of energy consumption and will consume around 5 times less electrical energy than small cryocoolers. But cryocoolers allow each wiggler to be operated independently from the others, which may increase the reliability of the CLIC damping rings. The CLIC damping rings should be designed with a certain amount of redundancy, that is, the emittance and damping time can also be met by using only a certain percentage of the damping wiggler magnets.

V. CONCLUSION

A conceptual design of superconducting damping wigglers for the CLIC damping rings was presented. Nb-Ti and Nb₃Sn superconducting CLIC damping wiggler magnets operated at 4.2 K meet the specifications. Hybrid-permanent magnet wiggler magnets cannot achieve the required magnetic fields. From the requirements of the CLIC damping rings, the gap size g , the period length λ_w and the minimal required magnetic flux density in the center of the gap B_w of the wiggler magnets are given. Then, the choice of the wiggler coil design, the choice of the strand technology (Nb-Ti or Nb₃Sn) and the choice of the wire bundle dimension was discussed in detail in this paper. By using the presented methods and figures the superconducting wiggler design becomes straight forward. The quench behavior is not critical, the dipole field quality in the wiggler magnets required for the damping rings can be met easily. Further, was discussed that operation at 1.9 K is only of limited advantage and will therefore not be pursued. After showing that the magnet design of wiggler magnets for the CLIC damping rings is feasible, the design was verified by building two Nb-Ti short models, which both reached short sample current. The usage of Nb₃Sn superconductor wire may increase the mid plane flux density B_w by 50%, leading to a better beam quality. However, the manufacturing of Nb₃Sn wiggler magnets is challenging due to the required heat treatment and the brittleness of the strand afterwards. The first trial coils showed that Nb₃Sn wiggler magnets are within the technological reach. The results will be published elsewhere.

The system integration of the superconducting damping wiggler was discussed in detail. Therefore, all known heat load sources from the beam and from operation are qualitatively and quantitatively discussed. Eddy currents and the heat load from resistive joints are small. The major source of heat load is beam-induced. Image currents and electron clouds can be kept small, but have contradictory requirements. To reduce the electron clouds, especially in the positron ring, the beam pipe should be coated with a material with small electron emission yield, usually a material with poor conductivity. On the other hand, for the reduction of image currents the surface of the beam pipe should have high conductivity. Surface treated grooved copper requires further studies. The most important beam induced heat load is from synchrotron radiation. In this paper an optimized absorber scheme is presented with the corresponding heat load from synchrotron radiation on the beam pipes of the wiggler magnets. Further, the calculation scheme for the heat load on the beam pipes of the wiggler magnets and the absorbers is derived and presented.

The heat load study is used to discuss the cooling concept. Standard bath cooling is not an option; therefore, an advanced cooling concept is presented and conceptually derived. Two large scale cooling concepts are presented and compared to each other. Large scale cryogenic

TABLE XII. Nomenclature for synchrotron radiation calculation

Symbol	Description
a, b	1/2 of beam pipe's x and y dimension
d	Distance
d_e, d_z	Element size in xy and xz -plane
k, l	Sequence number of wiggler and absorber
n, m	Number of elements in xy and xz -plane
p	Number of downstream wigglers
r_l, s_l	1/2 of l -th absorber's x and y dimension
$X_{i,j}, Y_{i,j}, Z_{i,j,k}$	Node's coordinates
θ, ψ	Angle between ray and xz and yz -plane
$\theta_{k,l}^{\max}, \psi_{k,l}^{\max}$	Max angle of k 's ray irradiating beam pipe
$\theta_{k,l}^{\max}, \psi_{k,l}^{\max}$	Max angle of k 's ray irradiating l

768 plants are favorable in terms of energy consumption and
 769 will consume around 5 times less electrical energy than
 770 small cryocoolers. But cryocoolers allow independent op-
 771 eration of each wiggler, which may increase the reliability
 772 of the CLIC damping rings. The technical concept will
 773 be tested at the ANKA storage ring in Karlsruhe.

774 Appendix A: Calculation method of synchrotron 775 radiation heat load

776 The radiation power emitted by an electron moving on
 777 a sinusoidal trajectory is [45, 46]:

$$\frac{dP}{d\Omega} = \frac{d^2P}{d\theta d\psi} = 3 \frac{\gamma^2}{\pi^2} P_T f_K(\gamma\theta, \gamma\psi), \quad (\text{A1})$$

778 where θ and ψ are the observation angles in the horizon-
 779 tal and vertical directions (Fig. 11), and P_T is the total
 780 power integrated over all angles and frequencies:

$$\{P_T\}_{\text{kW}} \approx 0.633 \{E\}_{\text{GeV}}^2 \{B_w\}_{\text{T}}^2 \{L\}_{\text{m}} \{I\}_{\text{A}}, \quad (\text{A2})$$

781 where L is the total length of the wiggler and I is the
 782 average current of the beam. The total dissipated power
 783 from one Nb-Ti wiggler magnet will be 14 kW.

784 Tab. XII describes the nomenclature used in the fol-
 785 lowing derivation. The angular dependence is given by:

$$f_K(\gamma\theta, \gamma\psi) = \int_{-\pi}^{\pi} \sin^2 \alpha \left(\frac{1}{D^3} - \frac{4(\gamma\theta - K \cos \alpha)^2}{D^5} \right) d\alpha, \quad (\text{A3})$$

787 where $D = 1 + (\gamma\psi)^2 + (\gamma\theta - K \cos \alpha)^2$ and the deflection
 788 parameter K is given by:

$$K = 0.934 \{\lambda_w\}_{\text{cm}} \{B_w\}_{\text{T}} \approx 15.7. \quad (\text{A4})$$

789 Equation (A1) cannot be integrated analytically and
 790 therefore a numerical method was developed to calculate
 791 the heat load on the beam pipe.

792 Fig. 18 shows the cross section of the elliptic beam
 793 pipe with the axes a and b . The ellipse is divided into a

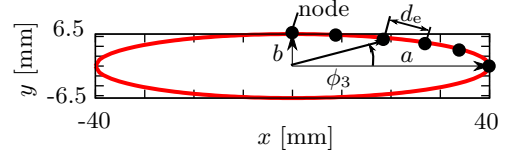


FIG. 18. Beam pipe ellipse.

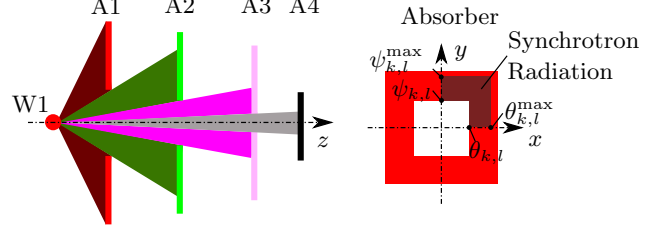


FIG. 19. Example for an absorber scheme. Left: Heat load from each wiggler magnet k (here $k = 1$) on each absorber l (here $l = 1, 2, 3, 4$). The heat load from additional wiggler magnets can be superimposed. Right: Absorber.

794 mesh of $4n$ equidistant segments with a length of $d_e = \frac{C}{4n}$
 795 (C is the circumference of the ellipse). In the example
 796 shown in Fig. 18 n is 5. In a next step it is investigated
 797 how much radiation hits the beam pipe segment from a
 798 downstream wiggler. In these calculations it is assumed
 799 that absorbers as shown in Fig. 19 are in position. A
 800 computer program was written to calculate the radiation
 801 generated in each longitudinal segment and also to calcu-
 802 late if and where the radiation hits the beam pipe. The
 803 total power deposited on the beam pipe is finally inte-
 804 grated and allows calculating the total deposited power
 805 on the vacuum chamber.

806 Appendix B: Heat load on absorbers

807 The heat load on each quadrant of the absorber l ir-
 808 radiated by each wiggler k can be calculated by triple
 809 numerical integration of Equation (A1). The positive
 810 boundaries $\theta_{k,l}$ and $\psi_{k,l}$ (Fig. 19) for the calculation of
 811 the positive quadrant are given by:

$$\theta_{k,l} = \arctan \frac{r_l}{d_{k,l}}, \quad (\text{B1})$$

$$\psi_{k,l} = \arctan \frac{s_l}{d_{k,l}}, \quad (\text{B2})$$

812 where $d_{k,l}$ is the distance between the wiggler k and the
 813 absorber l . The parameters r_l and s_l are the horizontal
 814 and vertical apertures of the absorber l .

815 The maximum angles $\theta_{k,l}^{\max}$ and $\psi_{k,l}^{\max}$ at which syn-
 816 chrotron radiation from wiggler k hits the absorber l is:

$$\theta_{k,l}^{\max} = \min_{i=[k,l-1]} \theta_{k,i} \quad \text{with} \quad \theta_{k,k} = \frac{\pi}{2}, \quad (\text{B3})$$

$$\psi_{k,l}^{\max} = \min_{i=[k,l-1]} \psi_{k,i} \quad \text{with} \quad \psi_{k,k} = \frac{\pi}{2}. \quad (\text{B4})$$

ACKNOWLEDGMENTS

The authors want to thank the involved members of the TE department for technical support and many valuable discussions. Special thanks are addressed to Juan Carlos Perez and Jacky Mazet for preparation of pieces and winding the CERN-KIT short model wiggler. We want to thank Giovanna Vandoni for discussions on vacuum issues and Antonio Perin for discussions on the cryogenic system. We want to thank Ezio Todesco for com-

ments on the paper. Bernardo Bordini we thank for performing short sample measurements. Attilio Milanese we want to thank for comments on the synchrotron radiation calculation. Emmanuele Ravaioli we want to thank for PSpice simulations. We would like to thank Denis Gurov, Anatoly Utkin, BINP and the BINP machine shop for their support in the design and manufacturing of the CERN-BINP short model. We would like to express our gratitude to Boris Podobedov, BNL, for discussions on the image current calculations.

-
- [1] CLIC, Website (2011), <http://clic-study.org>.
- [2] Tomás, R. (2010) *Phys. Rev. ST Accel. Beams* **13**(1), 014801.
- [3] Antoniou, F., *et al.*, International Particle Accelerator Conference (2010), pp. 3542–3544.
- [4] ANKA at Karlsruhe Institute of Technology, Website, <http://ankaweb.fzk.de>.
- [5] Rumolo, G., *et al.*, European Particle Accelerator Conference (2008), pp. 658–660.
- [6] Mezentsev, N. and Wallén, E. (2011) *Synchrotron Radiation News* **24**(3), 3–9.
- [7] Emma, P. and Raubenheimer, T. (2001) *Phys. Rev. ST Accel. Beams* **4**(2), 021001.
- [8] Korostelev, M., Optics design and performance of an ultra-low emittance damping ring for the compact linear collider, PhD thesis, Ecole polytechnique fédérale de Lausanne (2006).
- [9] CLIC parameter list 3 TeV (2010), <http://clic-meeting.web.cern.ch/clic-meeting/clicktable2010.html>.
- [10] Antoniou, F. and Papaphilippou, Y. European Particle Accelerator Conference (2008), pp. 685–687.
- [11] Opera Software Package, Cobham CTS Limited, 24 Bankside Kidlington Oxfordshire OX5 1JE, UK.
- [12] Bochvar Institute of Inorganic Materials, Moscow, Nb-Ti strand: Diameter bare 0.85 mm, insulated 0.92 mm, SC/Cu ratio 1.5/1, 630 A at 5 T, RRR 100, 330 Filaments (45 μm), www.bochvar.ru.
- [13] Oxford Instruments, Restacked Rod Process, diameter bare 0.81 mm, insulated 0.94 mm, SC/Cu ratio 1.1/1, 800 A at 12 T, RRR 300, 54 Filaments (80 μm), www.oxinst.com.
- [14] Bottura, L. (2000) *IEEE Trans. Appl. Supercond.* **10**(1), 1054–1057.
- [15] Kramer, E. (1973) *J. Appl. Phys.* **44**(3), 1360–1370.
- [16] Summers, L., *et al.* (1991) *IEEE Trans. Magn.* **27**(2), 2041–2044.
- [17] E. Wallén, (ed.) (2010) Insertion devices for rings and linacs. IDMAX2010, Workshop, Lund, Sweden, .
- [18] Safranek, J., *et al.*, (2002) *Phys. Rev. ST Accel. Beams* **5**(1), 010701.
- [19] Maccaferri, R., *et al.*, European Particle Accelerator Conference (2004), pp. 1630–1632.
- [20] B. Bordini, *et al.*, *IEEE Trans. Appl. Supercond.*, vol. 20, pp. 274–278, 2010.
- [21] Schoerling, D., *et al.*, International Particle Accelerator Conference (2010), pp. 3174–3176.
- [22] CERN, LHC design report volume I. The LHC main ring (2004).
- [23] Scheuerlein, C., Schoerling, D., and Heck, S. (2010) *IEEE Trans. Appl. Supercond.* **PP**(99), 1.
- [24] Schoerling, D., *et al.* (2011), "Electrical resistance of Nb₃Sn/Cu splices produced by electromagnetic pulse technology and soft soldering", accepted for publication, *Supercond. Science & Technology*.
- [25] Pippard, A. B. (1947) *Proc. R. Soc. Lond. A* **191**(1026), 385–399.
- [26] Reuter, G. E. H. and Sondheimer, E. H. (1948) *Proc. R. Soc. Lond. A* **195**(1042), 336–364.
- [27] Podobedov, B. (2009) *Phys. Rev. ST Accel. Beams* **12**(4), 044401.
- [28] Rumolo, G., Ruggiero, F., and Zimmermann, F. (2001) *Phys. Rev. ST Accel. Beams* **4**(1), 012801.
- [29] Alesini, D., CERN Accelerator School (2010).
- [30] Suetsugu, Y., *et al.*, International Particle Accelerator Conference (2010), pp. 2021–2023.
- [31] Palmer, M. A., *et al.*, International Particle Accelerator Conference (2010), pp. 1251–1255.
- [32] Wiedemann, H. (2007) Particle accelerator physics, Springer, Berlin, .
- [33] NISTIR 5632, (2010), www.nist.gov/physlab/data/xraycoef/index.cfm.
- [34] Fastowski, W., Petrowski, J., and Rowinski, A. (1970) Kryotechnik, Akademie Verlag, Berlin.
- [35] Frey, H. and Haefler, R. (1981) Tieftemperaturtechnik, VDI-Verlag, Düsseldorf.
- [36] Iwasa, Y. (2009) Case studies in superconducting magnets, Springer, New York.
- [37] Lebrun, P. (2004) In CERN-2004-008.
- [38] Vandoni, G. (2004) In CERN-2004-008.
- [39] NIST Cryogenic material properties Website (2010), www.cryogenics.nist.gov.
- [40] Barron, R. (1985) Cryogenic Systems, Oxford Science Publications, .
- [41] Strobridge, T. (1974) *National Technical Information Service*.
- [42] Claudet, S., *et al.*, Technical Report LHC-Project-Report-317 (1999).
- [43] Perin, A. Private communication CERN (2011).
- [44] Three cryocooler are used: (1) Cryomech Al325 <http://cryomech.com>, (2) SHI cryogenic groups CH-210 and (3) RDK-415D www.shicryogenics.com.
- [45] Schwinger, J. (1949) *Phys. Rev.* **75**(12), 1912–1925.
- [46] Kim, K.-J. (1986) *Nucl. Instrum. Methods Phys. Res., Sect. A* **246**(1-3), 67 – 70.